Biochimica et Biophysica Acta 1838 (2014) 429–437

Contents lists available at ScienceDirect

Biochimica et Biophysica Acta

journal homepage: www.elsevier.com/locate/bbamem

Biomembrane disruption by silica-core nanoparticles: Effect of surface functional group measured using a tethered bilayer lipid membrane

Ying Liu [a], Zhen Zhang [b], Quanxuan Zhang [c], Gregory L. Baker [c], R. Mark Worden [a,*]

[a] Department of Chemical Engineering and Materials Science, Michigan State University, East Lansing, MI 48824, USA
[b] Department of Statistics and Probability, Michigan State University, East Lansing, MI 48824, USA
[c] Department of Chemistry, Michigan State University, East Lansing, MI 48824, USA

ARTICLE INFO

Article history:
Received 11 June 2013
Received in revised form 10 September 2013
Accepted 12 September 2013
Available online 21 September 2013

Keywords:
Silica nanoparticle
Lipid bilayer
Electrochemical impedance
Resistance
Aggregation

ABSTRACT

Engineered nanomaterials (ENM) have desirable properties that make them well suited for many commercial applications. However, a limited understanding of how ENM's properties influence their molecular interactions with biomembranes hampers efforts to design ENM that are both safe and effective. This paper describes the use of a tethered bilayer lipid membrane (tBLM) to characterize biomembrane disruption by functionalized silica-core nanoparticles. Electrochemical impedance spectroscopy was used to measure the time trajectory of tBLM resistance following nanoparticle exposure. Statistical analysis of parameters from an exponential resistance decay model was then used to quantify and analyze differences between the impedance profiles of nanoparticles that were unfunctionalized, amine-functionalized, or carboxyl-functionalized. All of the nanoparticles triggered a decrease in membrane resistance, indicating nanoparticle-induced disruption of the tBLM. Hierarchical clustering allowed the potency of nanoparticles for reducing tBLM resistance to be ranked in the order amine > carboxyl ~ bare silica. Dynamic light scattering analysis revealed that tBLM exposure triggered minor coalescence for bare and amine-functionalized silica nanoparticles but not for carboxyl-functionalized silica nanoparticles. These results indicate that the tBLM method can reproducibly characterize ENM-induced biomembrane disruption and can distinguish the BLM-disruption patterns of nanoparticles that are identical except for their surface functional groups. The method provides insight into mechanisms of molecular interaction involving biomembranes and is suitable for miniaturization and automation for high-throughput applications to help assess the health risk of nanomaterial exposure or identify ENM having a desired mode of interaction with biomembranes.

1. Introduction

Engineered nanomaterials (ENM) exhibit desirable electronic, catalytic and photonic properties and are rapidly being introduced into diverse commercial products [1–4]. However, considerable evidence has been obtained through in-vitro [5] and in-vivo [6,7] studies that ENM can cause significant health risks [8,9]. The ENM can enter the body through multiple pathways, interact with cells and then induce cytotoxicity in a variety of ways, including disrupting membranes, denaturing proteins, triggering oxidative stress, inducing inflammation, etc. Currently, methods to assess health effects of ENM and to rapidly screen ENM for likely health risks are inadequate [10].

For ENM to trigger toxicity, they must interact with cell membranes [11]. A wide variety of interaction mechanisms are possible; the ENM could bind to the membrane, aggregate around the membrane, remove lipids from the membrane, become stably embedded in the membrane, pass through the membrane, create dynamic pores in the membrane, be endocytosed by the membrane, etc. [12]. An ENM's physicochemical properties are likely to strongly influence its interactions with biomembranes. Several reports have suggested that nanoparticle transport through biomembranes varies with the nanoparticles' surface charge and size [13–16]. Negatively charged nanoparticles were more rapidly taken up by adenocarcinoma lung cells than positively charged ones [17]. On the other hand, HeLa cells more rapidly endocytosed positively charged nanoparticles than negatively charged ones [18]. A recent review of the influence of surface properties of ENM on cellular interactions indicated that, in general, uncharged ENM interact less aggressively with cells, and that positively charged ENM are most efficient in crossing cell membranes [19]. Consistent with these findings, Yacobi et al. [14] observed that transcellular trafficking of positively charged, amidine-functionalized polystyrene nanoparticles (amidine-PNP) across primary rat alveolar epithelial cell monolayers was 20–40 times faster than that of negatively charged, carboxyl-functionalized PNP (COOH-PNP). Trafficking was shown not to occur via known

* Corresponding author. Tel.: +1 517 353 9015.
E-mail address: worden@egr.msu.edu (R.M. Worden).

0005-2736/$ – see front matter © 2013 Published by Elsevier B.V.
http://dx.doi.org/10.1016/j.bbamem.2013.09.007

major endocytic pathways, suggesting that such translocation may take place by PNP diffusion through the lipid bilayer of cell membranes [20].

Despite the importance of ENM–biomembrane molecular interactions, they are poorly understood. One challenge arises from the inherent complexity of cell membranes, which are composed of a lipid bilayer decorated with a variety of embedded proteins and other accessory molecules. The accessory molecules contribute functionalities needed for vital membrane processes, including energy generation, recognition, communication and selective molecular transport [21,22]. Furthermore, biomembrane composition and function vary between different parts of a cell and in different cell types [23]. Given the inherent complexity and diversity of intact biomembranes, it is difficult to carry out well defined experiments and test hypotheses about the role of specific biomembrane components during ENM–biomembrane interactions.

A promising, bottom-up approach to study ENM–biomembrane interactions is to use biomimetic interfaces containing a bilayer lipid membrane (BLM) and the minimum number of other membrane constituents needed to mimic desired biomembrane functions. Several BLM-based platforms have been developed. The planar bilayer lipid membrane (pBLM) method involves forming an unsupported BLM across a small aperture between two aqueous solutions. This approach provides natural biomembrane fluidity and lipid mobility. However, a pBLM is typically fragile and exhibits a short lifetime. The supported BLM (sBLM) method involves self assembling a BLM on a hydrophilic substrate, such as silica or mica [24]. This approach provides increased membrane stability but lacks an ion reservoir between the BLM and substrate, hindering the use of electrochemical methods to measure transmembrane ion transport across the membrane. In the tethered BLM (tBLM) method (Fig. 1(A)), lipid molecules are first chemically tethered to the substrate to establish a template for the tBLM's lower leaflet. Then, additional lipid molecules are added, typically by liposome rupture, to complete the tBLM. The tBLM features both improved BLM stability and an ion reservoir on both sides of the membrane [25–27]. Forming a tBLM on gold allows the use of electrochemical impedance spectroscopy (EIS) to measure the membrane's electrical resistance (R_m) [19,28]. The R_m value, which is a key measure of a biomembrane's physical integrity and lack of defects, can serve as a measure of ENM-induced biomembrane disruption [29].

Amorphous silica nanoparticles represent an excellent model ENM for systematic studies of ENM–biomembrane interactions, because they are commonly found in nature, are widely used in commercial products [30], and are being developed as cargo carriers in targeted drug delivery [31–33]. Compared to crystalline silica particles, which if inhaled can cause pulmonary silicosis [34], amorphous silica nanoparticles are much less toxic to the lung. Inhalation of amorphous silica triggers minimal pulmonary inflammation in rodents [35]. The nanotoxicity properties of amorphous silica nanoparticles have been shown to vary with their size [36], structure [37] and surface properties [19,38], which can readily be customized via chemical functionalization. Pore formation in synthetic BLM composed of L-α-dimyristoyl phosphatidylcholine (DMPC) induced by silica nanoparticles less than 22 nm in size has been monitored by atomic force microscopy (AFM) [39].

The purpose of this study was to test the hypothesis that a tBLM-based method could be used to distinguish patterns of biomembrane disruption caused by nanoparticles that had identical amorphous-silica cores but different surface functional groups. EIS was used to measure time-dependent changes in the R_m of a highly insulating tBLM following exposure to three types of silica-core nanoparticles: bare, amine-functionalized, and carboxyl-functionalized. The rate of decrease in R_m was described using an exponential model, and hierarchical clustering was applied to statistically analyze whether the method could distinguish between the effects of different silica-core ENM. Dynamic light scattering (DLS) was used to measure changes in the nanoparticles' effective diameter before and after interactions with the tBLM. The results demonstrate the suitability of the tBLM method to screen ENM for aggressiveness in biomembrane disruption.

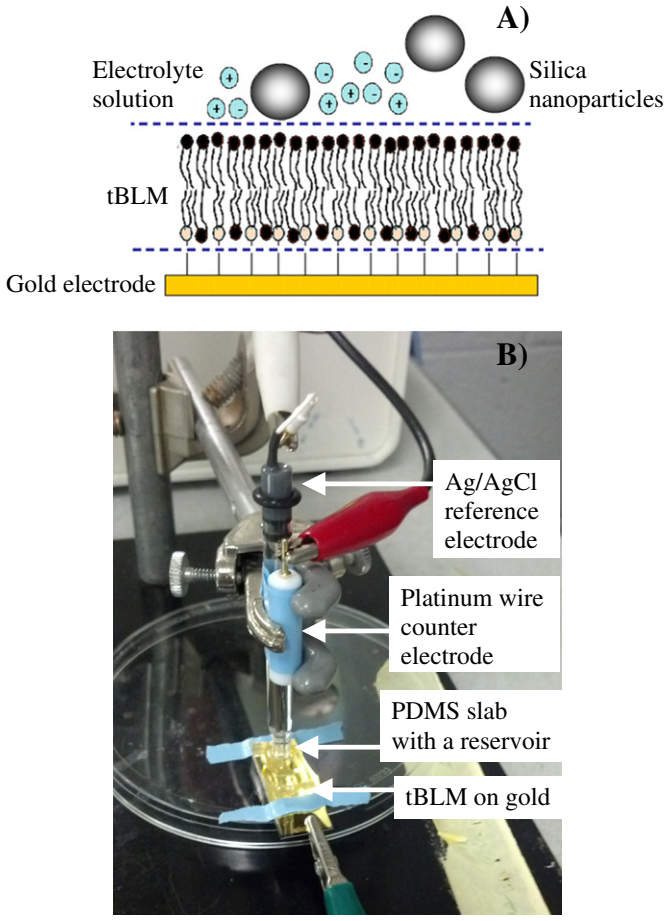

Fig. 1. (A) Schematic diagram of tBLM interaction with silica-core nanoparticles; (B) three electrode setup for EIS measurement.

2. Material and methods

2.1. Materials

Chloroform-solubilized 1,2-dioleoyl-*sn*-glycero-phosphocholine (DOPC) and 1,2-dipalmitoyl-*sn*-glycero-phosphothioethanol (DPPTE) in form of sodium salt were purchased from Avanti Polar Lipids (Alabaster, AL). All other chemicals, including NaCl, KCl, $CaCl_2$ and 4-(2-hydroxyethyl)-1-piperazineethanesulfonic acid (HEPES), were obtained from Sigma Aldrich (St. Louis, MO). All aqueous solutions were prepared in deionized (DI) water (18.2 MΩ) supplied by a Nanopure-UV four-stage purifier (Barnstead International, Dubuque, IA). Sylgard 184 silicone elastomer to prepare polydimethylsiloxane (PDMS) slab was purchased from Ellsworth Adhesives (Germantown, WI). Reference electrodes of silver/silver chloride and platinum counter electrodes were purchased from Bioanalytical Systems (West Lafayette, IN). All nanoparticles dispersed in DI water were stored at 4 °C at a concentration of 10 mg/mL.

2.2. Formation of tBLM on gold substrate

Electrodes consisting of a gold layer (100 nm thick) coated on a silicon wafer by chemical vapor deposition (Lance Goddard Associates, Santa Clara, CA) were cleaned in fresh piranha solution (51% H_2SO_4

and 30% H_2O_2 in a ratio of 7:3) for 30 s, washed with deionized water and then dried in nitrogen. A self-assembled monolayer (SAM) of DPPTE was chemically adsorbed by dipping a clean gold electrode into 1 mM ethanolic DPPTE solution for 1 h, rinsing with ethanol, and drying with nitrogen. Preparation of polydimethylsiloxane (PDMS) slabs with a cut-out reservoir is described in the supplementary material.

Small unilamellar vesicles (SUV) of DOPC were prepared by freeze drying DOPC dissolved in chloroform in a Labconco freeze dry system (Labconco Corporation, Kansas, MO) at −47 °C for 2 h followed by hydration in HEPES buffer (10 mM HEPES, 150 mM NaCl, 2 mM $CaCl_2$, pH 7.4) to a concentration of 1 mM. After ultrasonication for 20 min, 300 μL of the resulting SUV suspension was added to the PDMS slab reservoir and incubated at room temperature for 24 h. After tBLM formation, the liposome solution was replaced with fresh 10 mM KCl electrolyte (pH 6.1). Then sonicated nanoparticle solution was transferred to the PDMS reservoir and mixed by a pipette to reach a final concentration of 300 μg/mL in 10 mM KCl. In some control experiments, the volume of DOPC and nanoparticles transferred to the PDMS reservoir was varied, but the nanoparticles were maintained at the same concentration (300 μg/mL in 10 mM KCl) in all experiments.

2.3. Electrochemical impedance spectroscopy (EIS)

A BLM's lipid core blocks ion diffusion and thereby provides biomembranes with inherently high R_m values (order of MΩ cm^2). Molecules that disrupt or induce pores in BLM, such as channel proteins, ionophores, and some bacterial toxins, reduce R_m while maintaining membrane capacitance roughly constant [40–42]. In this study, EIS was used to measure changes in R_m during 5 h incubation with 300 μg/mL silica-core nanoparticles. A supporting electrolyte of 10 mM KCl was chosen because it provided sufficient conductance for the EIS studies while not inducing significant nanoparticle aggregation. EIS experiments were conducted using a CHI 660B electrochemical workstation (CH Instruments Inc., Austin, TX) configured in a three-electrode setup (Fig. 1(B)). An ac perturbation of 5 mV was superimposed on dc bias of 0 V over a frequency (ω) range between 0.01 Hz and 10,000 Hz. Experiments were conducted in triplicate for each type of nanoparticle, including the control groups. To determine R_m values, a modified Randles equivalent circuit (Fig. 2(A)) was fit to the electrical impedance (Z) data [43,44] using Zview software (Scribner Associates, Southern Pines, NC). A constant-phase element (CPE) was used in this modified model to represent electrical behavior of heterogeneous sub-membrane space [45,46].

2.4. Atomic force microscopy (AFM) imaging of tBLM

A DPPTE/DOPC tBLM was formed using the procedure described above on a 1 cm × 1 cm piece of freshly cleaned gold. AFM imaging experiments were performed in tapping mode using an Asylum Research Cypher Scanning Probe Microscope (Santa Barbara, CA) equipped with a droplet cantilever holder. A drive ω of ~30 kHz and spring constant of 0.01 N/m for the silicon nitride cantilever were determined by thermal data. After tBLM formation, the liposome suspension was exchanged with DI water before AFM scanning.

2.5. Fabrication and characterization of silica-core nanoparticles

The silica-core nanoparticles were fabricated from colloidal silica (SNOWTEX 20L (Nissan Chemical Industries, Ltd. SNT20L, 40–50 nm, 20 wt.% suspension in H_2O) as described in the supplemental information.

Because ENM aggregation can be affected by medium composition, especially electrolyte concentration [5,47], DLS was performed to identify an aqueous medium for the experiments that did not induce aggregation. In addition, particle size distributions were measured before and after ENM exposure to the tBLM [48]. Effective diameter and surface

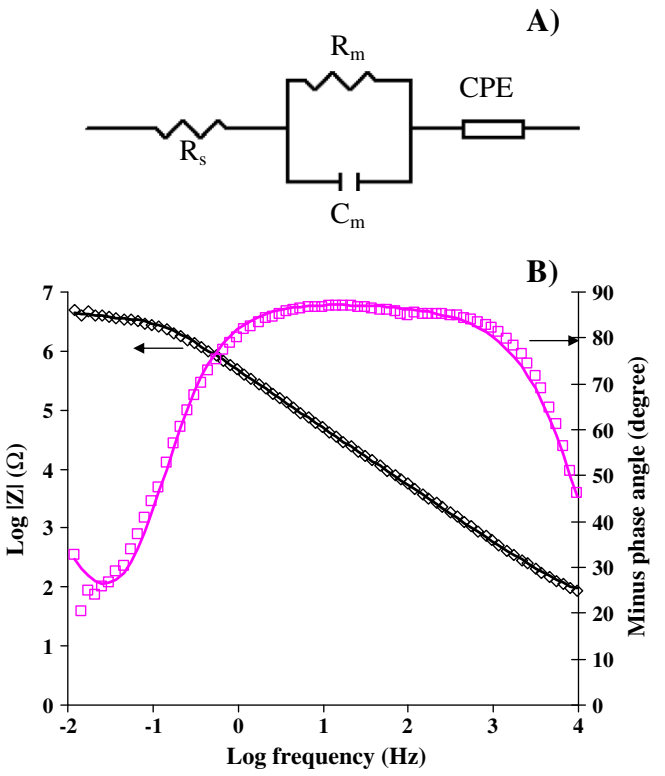

Fig. 2. (A) Modified Randles equivalent circuit that consists of an electrolyte solution resistance R_S, a membrane capacitance, C_m, a membrane resistance, R_m, and a constant-phase element, CPE, which dominates the hydrophilic spacer region. (B) Experimental and predicted EIS spectra of tBLM formed on 0.45 cm^2 gold. Left vertical axis: log of impedance (Z) magnitude (diamonds). Right vertical axis: minus phase angle (squares). Solid curves are impedance curves simulated from modified Randles equivalent circuit using Zview software.

charge (zeta potential) of functionalized silica-core nanoparticles were determined using a Brookhaven 90 Plus particle analyzer (Brookhaven Instruments Inc., Holtsville, NY) at 25 °C in 10 mM KCl. In control experiments to determine conditions that triggered nanoparticle aggregation, bare silica nanoparticles were incubated in 10 mM KCl in a glass cuvette, in a PDMS reservoir only, and in a PDMS reservoir on gold without tBLM, before particle-size analysis.

2.6. Statistical analysis

An exponential function Eq. (1) was fit to the R_m vs time profiles measured during exposure to silica-core nanoparticles,

$$R_m = (R_i - R_f)\exp(kt) + R_f \quad (1)$$

where R_i is the initial resistance, R_f is the final resistance, and k is the exponential rate constant. A relative membrane resistance change (R_m%) was also calculated using Eq. (2):

$$R_m\% = (R_i - R_f)/R_i. \quad (2)$$

A pattern matrix containing a total of n = 12 experiments as rows, and p = 3 parameters, ($R_i - R_f$), k, and R_m%, determined for each experiment as columns, was analyzed using hierarchical clustering procedures in R software (Version 2.13.2: The R Foundation for Statistical Computing), to quantify similarity between the curves. For hierarchical clustering, the distances between rows (experiments) when forming the clusters were calculated using Euclidean distance measured by summing the squared differences between rows over all columns (parameters). Since the parameters have scales in quite different orders

of magnitude, the scales were standardized [49] prior to the clustering procedure to prevent a parameter with larger order of magnitude from dominating the clustering results. Also, Ward's method was used to evaluate Euclidean distances and to determine which clusters should be linked together at each step in the dendrogram. Since the number of sample points (experiments) to be clustered was relatively small, the uncertainty associated with the hierarchical clustering results was assessed by computing the approximately unbiased (AU) p-value via multiscale bootstrap resampling [50] with replacement at each bifurcation. AU p values provide quantitative assessment of confidence in each clustering step. AU p values close to 100% indicate relative certainty that the clustering is true. Two-sample *t* test assuming unequal variance and Wilcoxon rank sum test were performed to compare size and surface charge of silica-core nanoparticles before and after tBLM experiments. Differences were considered significant at $p < 0.05$.

To identify whether measured changes in R_m following silica-core nanoparticle exposure were significant, the random fluctuation (noise) was estimated from the three control-group replicates that were not exposed to nanoparticles. The observations were assumed to be random samples from a normal distribution, and the variance was estimated using the pooled data from three control replicates (each with mean subtracted) to represent the random fluctuation. To validate the assumption, the Ljung–Box test [51] was used to test the potential serial correlation (randomness). Next, the normality condition for individual replicate of control group was tested using Shapiro–Wilk test [52]. Finally the homogeneity of variances across three replicates was assessed using Bartlett's test [53]. For all tests the p-values were greater than 0.05, indicating the corresponding assumptions hold at the 95% confidence level. After validating all assumptions, variances from three control replicates were pooled to estimate one single variance to represent the fluctuation.

3. Results

3.1. Characterization of dispersed silica-core nanoparticles before interaction with tBLM

The various functionalization chemistries resulted in some measurable differences in zeta potential and average diameter as measured by DLS. Fig. 3 shows effective diameter (Fig. 3(A)) and zeta potential (Fig. 3(B)) of bare, carboxyl-functionalized, and amine-functionalized silica nanoparticles before interaction with the tBLM. Bare silica had a diameter of 51.9 ± 6.5 nm and a zeta potential of −14.8 ± 3.0 mV. Carboxyl-functionalized silica had an effective diameter of 69.9 ± 4.4 nm and zeta potential of −16.0 ± 3.0 mV, respectively. Amine-functionalized silica had an effective diameter 111.0 ± 2.7 nm and a zeta potential (−29.7 ± 1.7 mV). Two-sample *t* test indicated that the average size and zeta potential values of amine silica were significantly different from those of either bare silica or carboxyl silica, while carboxyl silica did not show a difference from bare silica for size or

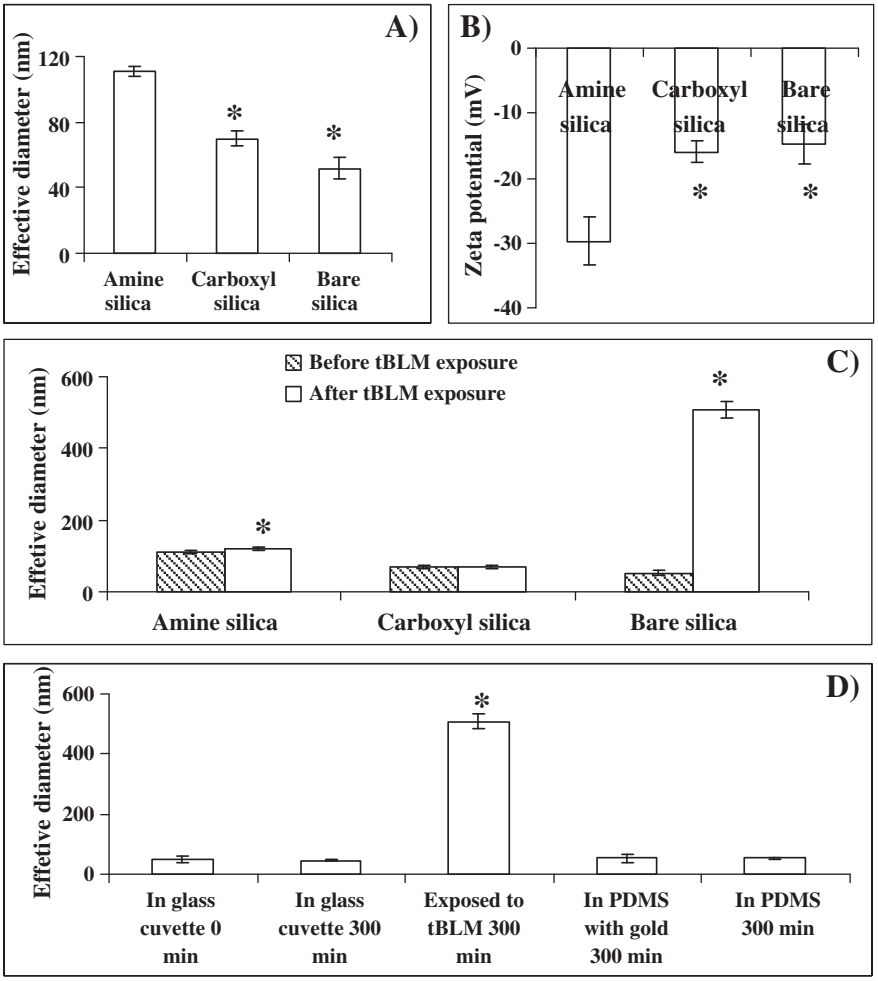

Fig. 3. (A) Size and (B) zeta potential of silica-core nanoparticles in 10 mM KCl before interaction with tBLM. An asterisk indicates significant difference between effective diameter or zeta potential of carboxylic acid or bare silica and amine silica. (C) Effective diameter of silica-core nanoparticles before and after 5 h interaction with tBLM, measured by DLS. An asterisk indicates significant difference of effective diameter of silica nanoparticles between before tBLM exposure and after. (D) Effective diameter of bare silica nanoparticles under various conditions by DLS. The asterisk indicates that the size of bare silica measured in the presence of tBLM is significantly higher than that measured in all other conditions.

zeta potential. The unexpected larger size and negative charge of the amine-functionalized nanoparticles are believed to be due to cross-linking of two or more nanoparticles via adsorption of a multivalent anion onto the aminated surface. Candidate multivalent anions include SO_4^{2-}, which was the counterion for the Cu^{2+} click chemistry catalyst, and $EDTA^{4-}$, which was added in excess to remove the Cu^{2+} catalyst following the reaction. Stable adsorption of oppositely charged polyelectrolytes has been reported to reverse the zeta potential of charged particles and to encourage aggregation by creating ionic bridges between adjacent particles [54].

3.2. AFM imaging and electrochemical characterization of tBLM

Tapping-mode AFM images of a DPPTE/DOPC tBLM in DI water (Fig. 4(A)) and the bare gold substrate in water (Fig. 4(B)) have a similar appearance. The tBLM's surface roughness, 1.16 ± 0.00032 nm, agrees well with that reported (0.9 ± 0.2 nm) for a densely packed tBLM [55] and is not statistically different from that of bare gold substrate (1.12 ± 0.0085 nm). This result is consistent with formation of a conformal BLM on the gold that is uniform and homogeneous.

Impedance analysis was used to investigate the integrity of the tBLM. The presence of small defects (holes) in the tBLM would allow local contact between the electrolyte solution and the electrode. The overall R_m of the tBLM may be calculated by considering the tBLM-coated regions and the defect regions as distinct conductive paths in parallel. Because the resistivity of a phospholipid bilayer (about 10^{12} Ω cm) is about 10 orders of magnitude higher than that of the 10 mM KCl electrolyte solution (about 70 Ω cm) [56,57], the overall R_m of a tBLM is extremely sensitive to small defect areas. For example, addition of a defect area fraction as low as 1.8×10^{-13} to a previously defect-free tBLM would result in 50% reduction in the R_m value. This inherent sensitivity helps to explain the variation in initial R_m values before nanoparticle exposure seen among replicates, as well as the method's ability to detect changes in R_m following nanoparticle exposure (Fig. 5). Because such a low area fraction could not be discerned in an AFM image, the height variations observed in Fig. 4(A) are likely due to roughness in the underlying electrode, rather than defects in the tBLM.

Fitting the equivalent circuit model (Fig. 2(A)) to a typical set of tBLM impedance data gave an R_m value of 1.5 MΩ cm^2 and a C_m value of 0.84 μF/cm^2 (Fig. 2(B)). These values compare favorably with literature values, which range between 0.1 and 15 MΩ cm^2, [26,40,41,58–60], providing further evidence of a highly insulating tBLM.

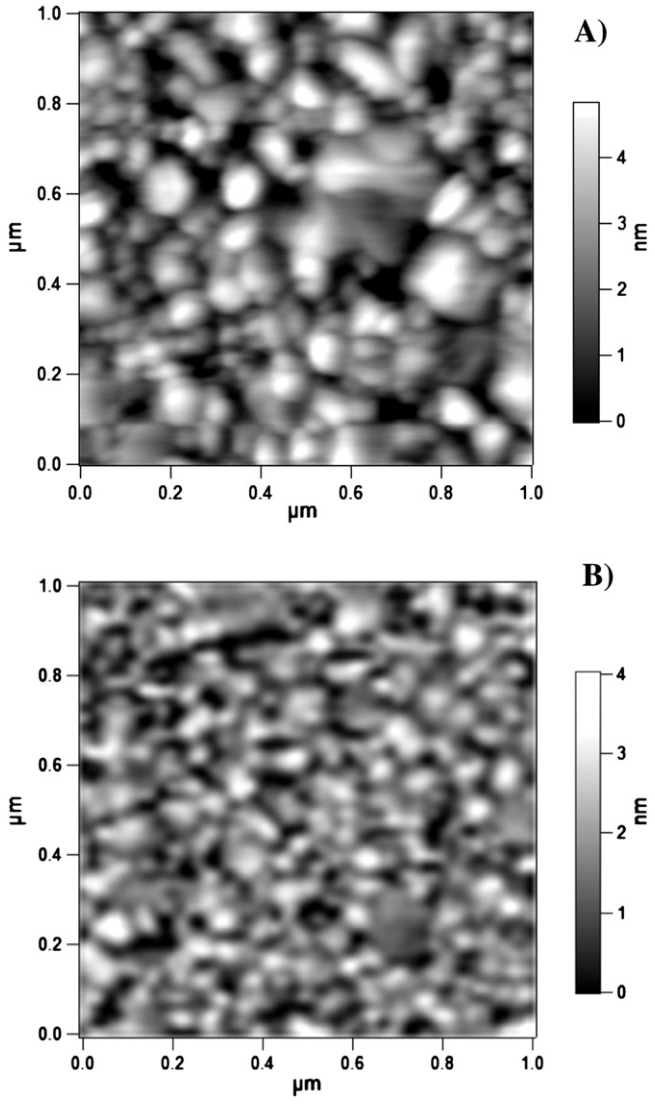

Fig. 4. AFM height images of tBLM (A) and bare gold substrate (B).

3.3. Effects of silica-core nanoparticles on membrane resistance of tBLM

Fig. 5(A) shows triplicate R_m vs. time curves for the control runs performed without nanoparticles, as well as the runs conducted with 300 μg/mL of silica-core nanoparticles having different functional groups. A Ljung–Box test shows all p-values (Table 1 in supplementary material) greater than 0.05 for control groups at lags ranging from one to five, so that the serial correlation shows non-significance and randomness assumption holds well. Thus, observations can be treated as random samples for each of the three replicates of control groups. Similarly, the Shapiro–Wilk test shows non-significance (p-value 0.84, 0.25 and 0.90, respectively), indicating that the normality assumption holds for all three replicates. Then, the Bartlett's test of homogeneity of variances shows non-significance (p-value 0.06), and the three replicates are roughly considered to have the same variance. Thus, the data from individual replicates were pooled to obtain the common standard deviation, which represents the fluctuation level to be 0.062 MΩ cm^2 with 95% confidence interval. Fluctuations in initial R_m values among experiments are believed to result from differences in roughness of the gold substrates after cleaning with piranha solution [40]. Although piranha treatment enhances the electrocatalytic activities of gold electrode, AFM and SEM studies also demonstrated piranha treatment could substantially increase gold electrode roughness [61,62].

In all runs shown in Fig. 5(B)–(D), the final R_m values were smaller than the initial values, indicating an enhanced ability of ions to traverse the tBLM after exposure to the silica-core nanoparticles. For the bare silica and carboxyl-functionalized nanoparticles, the rates of R_m decline could be accurately traced using a 30 min interval between R_m measurements. However, for the amine-functionalized nanoparticles, virtually the entire drop in R_m occurred within the first 30 min (Fig. 5(C)). To more accurately estimate the exponential rate constant (k in Eq. (1)) for these nanoparticles, EIS was performed over a smaller ω range (from 0.1 Hz to 10,000 Hz), reducing the sampling period by a factor of 15. The use of a two minute sampling interval allowed the rate of R_m decline to be more clearly resolved for the amine silica (Fig. 5(E)).

Clustering analysis was then used to test the hypothesis that the tBLM method could distinguish patterns of biomembrane disruption caused by nanoparticles that had identical amorphous-silica cores but different surface functional groups. Eqs. (1) and (2) were fit to R_m vs. time profiles (Fig. 5). Then, the clustering analysis was applied to the resulting three values of ($R_i - R_f$), k, and R_m%. The dendrogram generated from hierarchical clustering using a parameter matrix containing best-fit ($R_i - R_f$), k, and R_m% values (Fig. 6) visually displays the degree of similarity between experiments. Numbers below the line indicate the

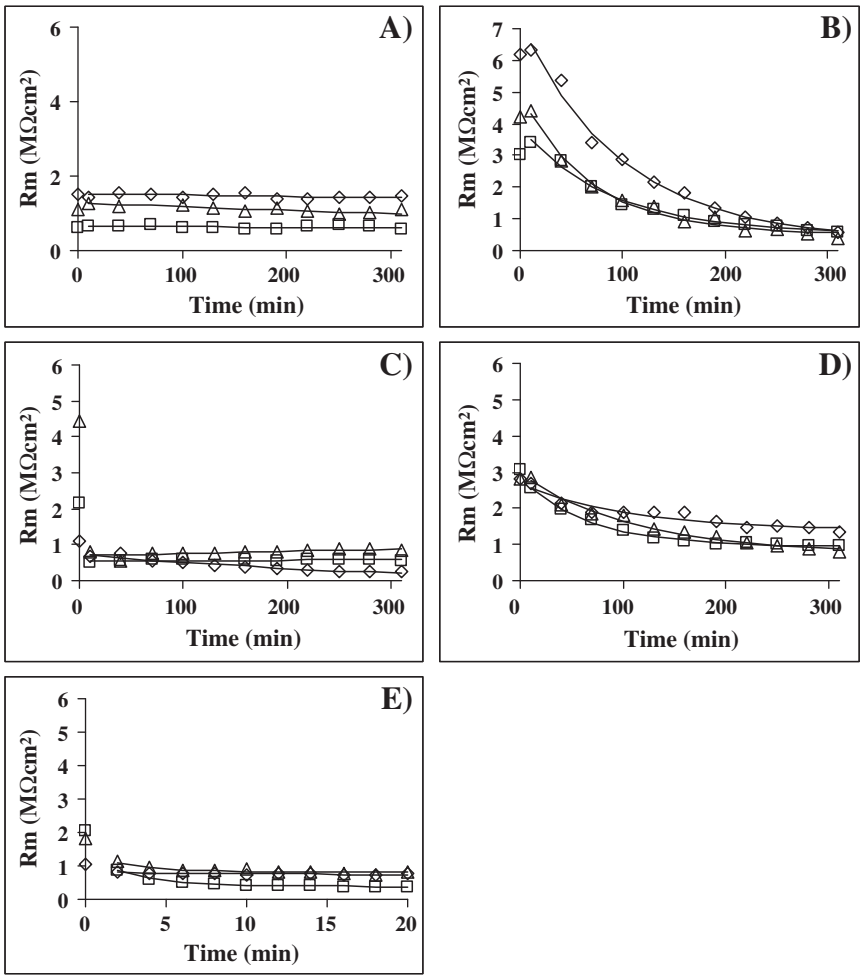

Fig. 5. Membrane resistance time profiles during tBLM interaction with 300 μg/mL bare and functionalized silica-core nanoparticles in 10 mM KCl. The addition of (A) an aliquot of water (control), (B) carboxyl functionalized silica, (C) amine functionalized silica, (D) bare silica, and (E) amine functionalized silica nanoparticles was performed immediately after first R_m recorded for each replicate. Open points are experimental values, and curves are optimized exponential model fits.

sequence in which two objects are linked together, while numbers above the line are AU p values at every clustering step.

The dendrogram indicates that each type of nanoparticle clusters as a unique group, consistent with the hypothesis. When only R_m data acquired at 30-minute intervals (Fig. 5(A)–(D)) were used to calculate ($R_i - R_f$), k, and R_m% values, the amine silica nanoparticles clustered most closely with the control group (Fig. 6(A)), because 30-min sampling interval did not capture the rapid exponential decline in R_m that is apparent in Fig. 5(E). However, when the two-min sampling interval R_m profiles for amine silica nanoparticles (Fig. 5(E)) were used, the resulting dendrogram (Fig. 6(B)) showed little similarity between the amine silica nanoparticles and the other three cases. Also, Fig. 6(B) shows higher AU p values than those in Fig. 6(A), indicating a greater degree of certainty that the clusters are distinct.

3.4. Effects of tBLM exposure on aggregation of silica-core nanoparticles

Fig. 3(C) shows effective diameter of bare, amine-functionalized, and carboxyl-functionalized nanoparticles measured before and after interaction with tBLM. Both two-sample *t* test and Wilcoxon rank sum tests indicated a significant difference between the size of bare and amine-functionalized silica before and after exposure to the tBLM. However, the size of carboxyl-functionalized silica did not change significantly during tBLM exposure. Control experiments were conducted to identify whether the apparent aggregation of bare silica nanoparticles may have been due to factors other than the tBLM exposure. Final particle sizes measured following 300 min contact of the bare silica nanoparticles with the glass cuvette, the PDMS well, the PDMS well with a gold electrode, and the PDMS well with a gold electrode covered with a tBLM, respectively, are shown in Fig. 3(D). Statistical analysis indicated no significant difference before and after exposure of the bare silica nanoparticles to all components tested, except the tBLM.

4. Discussion

The dendrogram's ability to cluster silica-core nanoparticles according to their surface functional groups confirms the study's central hypothesis. Thus, this study demonstrates for the first time that a tBLM method can measure time-dependent changes in tBLM R_m values with sufficient sensitivity to discern differences in potency of BLM disruption by ENM that are identical except for their surface functional groups.

Although bare silica, carboxyl silica, and amine silica particles all caused a decrease in R_m that was well represented by an exponential curve, other trends in nanoparticle-induced R_m dynamics have also been observed. For example, when the same silica-core nanoparticles were functionalized with short polyethylene glycol (PEG) functional groups, the resulting PEG-functionalized silica nanoparticles triggered a minor increase in the tBLM resistance (data not shown). Because these R_m trajectories were poorly described by the exponential decay

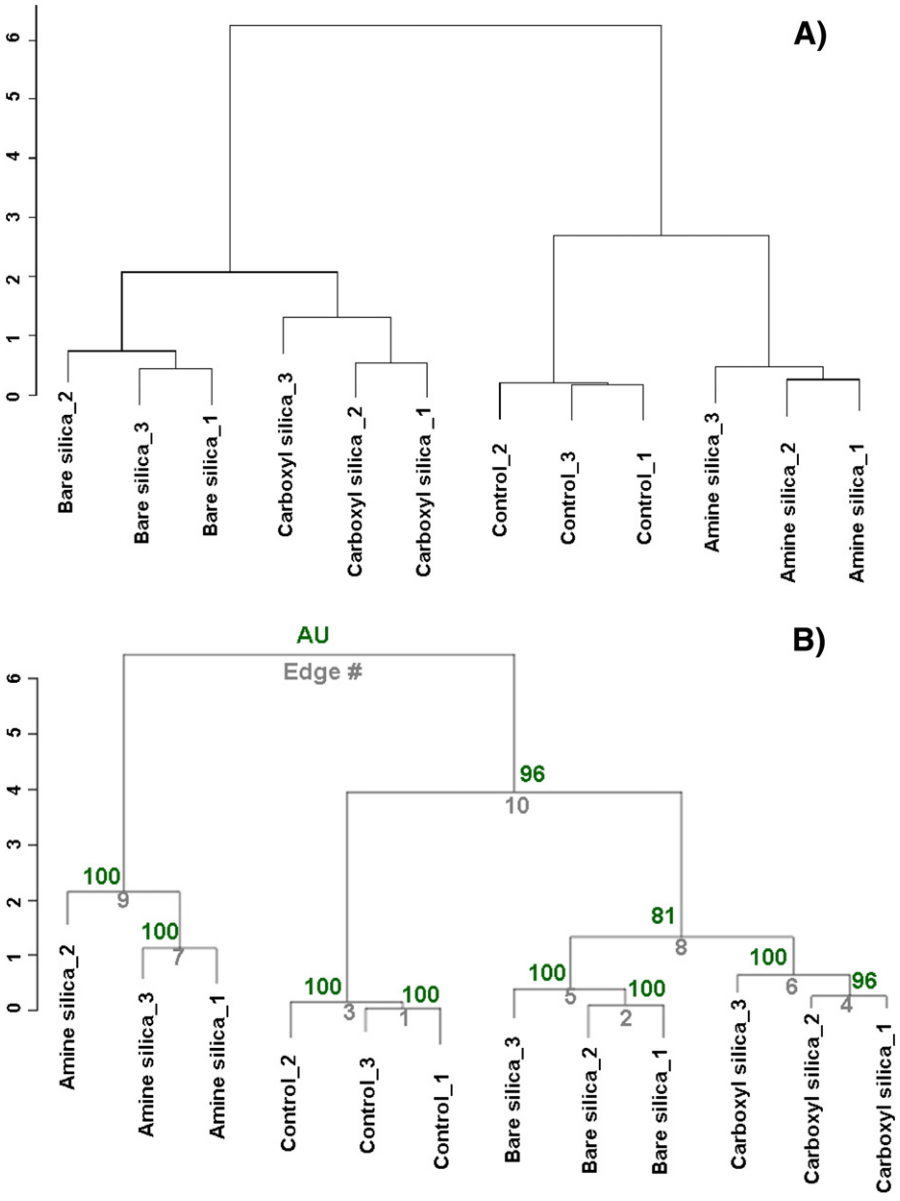

Fig. 6. Hierarchical clustering dendrogram resulting from Ward's method analysis of Fig. 5 data. Parameters for dendrogram were analyzed Fig. 6(A) from data in Fig. 5(A)–(D), and Fig. 6(B) from data in Fig. 5(A), (B), (D), and (E). The sequence of clustering steps is shown below the line, and the AU p-value for each clustering step is shown above the line. The vertical axis is a measure of the distance between the members of each clustered set.

model (Eq. (1)) and were easily distinguishable from the trajectories of the other three silica-core nanoparticles, the PEG-functionalized nanoparticle data were not included in the clustering analysis.

At this time, molecular interaction mechanisms between the ENM and tBLM are insufficiently understood to unambiguously map the R_m trajectories into detailed knowledge of ENM–biomembrane interactions. Additional research is needed to calibrate the tBLM in terms of underlying mechanisms. Nevertheless, trends in the experimental results presented here provide reproducible measures of molecular–scale interactions. One hypothesis to explain the decline in R_m is that nanoparticles adsorb to the tBLM and then remove lipids, thereby generating or enlarging defects in the tBLM through which ions could traverse the tBLM. This hypothesis is consistent with the observed increase in effective diameter of bare and amine-functionalized silica following exposure to the tBLM. Lipid transferred from the tBLM to the nanoparticles could trigger nanoparticle cross-linking and aggregation. The hypothesis is also consistent with reports that PAMAM dendrimers removed lipid from an sBLM on a carbon electrode, thereby reducing R_m measured by EIS and increasing Faradaic current measured by cyclic voltammetry [63]. Additional evidence for BLM lipid removal has been provided by AFM images showing holes in sBLM on mica induced by dendrimers [64–66], as well as by visible microscopy images showing disruption of a sBLM by semihydrophobic nanoparticles [67]. Finally, de Planque et al. have shown that both bare silica and amine-functionalized silica nanoparticles induced current spikes in DOPC planar BLM and reduced the lifetime of the BLM [68].

Mechanistic insight into nanoparticle–bilayer interactions can be difficult to discern when using intact cell membranes, because the nanoparticles may interact with intact cell membranes through a variety of mechanisms [19], some of which involve protein-mediated events. For example, in receptor-mediated endocytosis, highly selective membrane receptor proteins may bind a target macromolecule and trigger endocytosis [69]. Results of this study showed not only that silica-core nanoparticles can disrupt biomembranes through direct action on the lipid bilayer, as evidenced by a significant reduction in the tBLM's R_m value, but that the potency of disruption can be significantly affected

by the surface chemistry of the otherwise identical nanoparticles. This finding suggests that it may be possible to achieve highly selective macromolecule–biomembrane interactions without the need for protein-mediated processes.

The simple exponential model (Eq. (1)) did a reasonable job of describing the R_m trajectories for the bare, carboxyl-functionalized, and amine-functionalized nanoparticles, and the regression constants are physically meaningful. Specifically, $(R_i - R_f)$, k, and R_m%, represent the total change, the rate of change, and the fractional change in R_m as a function of time. This physical interpretation provides a framework by which nanoparticles may be ranked in order of potency for biomembrane disruption. The parameter regression constants for amine, carboxyl, and bare silica, combined with the observation that PEG-functionalized silica-core nanoparticles did not reduce R_m, yield the following potency rank for functionalized amorphous silica EMN: amine > carboxyl ~ bare silica > PEG.

The hierarchical clustering method presented here could be extended to models other than Eq. (1), such as one capable of describing an initial increase in R_m followed by a decrease. In addition to different models, different combinations of variables could be analyzed in the clustering analysis. We found that including all three variables: k, $(R_i - R_f)$ and R_m% allowed effects of different nanoparticles to be better distinguished than when only two (k and either $(R_i - R_f)$ or R_m%) were used.

Finally, the utility of the tBLM model for characterizing ENM–biomembrane interactions can be assessed in comparison to the pBLM method, which has been adapted from the field of electrophysiology [29]. The pBLM method has considerably greater sensitivity and dynamic range, allowing dynamics of individual pores in a pBLM to be characterized with current resolution on the order of pA and temporal resolution on the order of ms. However, the tBLM structure is more robust and uses less expensive equipment. Moreover, because the tBLM is formed by molecular self-assembly, the tBLM method is suitable for automated, robotic operation, and it can be miniaturized onto microfabricated electrode arrays for high-throughput applications. Thus, the tBLM method appears well suited to help assess ENM for biomembrane interactions and to rapidly screen ENM libraries for those giving desirable functional and biosafety profiles.

5. Conclusions

The novel method presented here integrates EIS to monitor the R_m of a tBLM during nanoparticle exposure, an exponential-decay model to describe R_m vs time trajectories, and statistical hierarchical clustering to generate a dendrogram that graphically depicts similarities of time trajectories due to different nanoparticles. The R_m profiles obtained while challenging a tBLM composed of DPPTE/DOPC with three types of amorphous-silica-core nanoparticles (bare, amine-functionalized, and carboxyl-functionalized) could be reasonably described with a decaying exponential model. The resulting dendrogram successfully clustered each set of replicates and confirmed the study's central hypothesis that a tBLM-based method could be used to distinguish patterns of biomembrane disruption caused by nanoparticles that had identical amorphous-silica cores but different surface functional groups. The results also allowed the tBLM-disrupting potency of the surface-functionalized silica nanoparticles to be ranked in the decreasing order amine > carboxyl ~ bare silica, with PEG-functionalized nanoparticles not reducing the R_m. These findings indicate that nanoparticle surface chemistry (e.g., click chemistry) can be used to modify the nanoparticles' surface functional group and thereby modulate nanoparticle–biomembrane interactions. Changes in the surface functional group also influenced the tendency of silica nanoparticles to aggregate following exposure to a tBLM; bare silica nanoparticles aggregated significantly, while carboxyl-functionalized nanoparticles showed no change in diameter. The methods presented here are generic and could be applied to a wide range of nanoparticles and tBLM compositions to test other hypotheses about nanomaterial interactions with biomembranes.

Supplementary data to this article can be found online at http://dx.doi.org/10.1016/j.bbamem.2013.09.007.

Acknowledgements

This manuscript is in memory of our colleague Dr. Gregory L. Baker who passed away unexpectedly while this paper was being written. Dr. Baker was responsible for the generation and characterization of the nanoparticles used in this study. This research was funded by NIH 5RC2ES018756-02.

References

[1] I. Brigger, C. Dubernet, P. Couvreur, Nanoparticles in cancer therapy and diagnosis, Adv. Drug Deliv. Rev. 54 (2002) 631–651.
[2] J.F. Hicks, D.T. Miles, R.W. Murray, Quantized double-layer charging of highly monodisperse metal nanoparticles, J. Am. Chem. Soc. 124 (2002) 13322–13328.
[3] N.J. Walker, J.R. Bucher, A 21st century paradigm for evaluating the health hazards of nanoscale materials? Toxicol. Sci. 110 (2009) 251–254.
[4] D.B. Warheit, Debunking some misconceptions about nanotoxicology, Nano Lett. 10 (2010) 4777–4782.
[5] G. Oberdorster, A. Maynard, K. Donaldson, V. Castranova, J. Fitzpatrick, K. Ausman, J. Carter, B. Karn, W. Kreyling, D. Lai, S. Olin, N. Monteiro-Riviere, D. Warheit, H. Yang, Principles for characterizing the potential human health effects from exposure to nanomaterials: elements of a screening strategy, Part. Fibre Toxicol. 2 (2005) 8.
[6] I.L. Hsiao, Y.J. Huang, Titanium oxide shell coatings decrease the cytotoxicity of ZnO nanoparticles, Chem. Res. Toxicol. 24 (2011) 303–313.
[7] N. Li, J.R. Harkema, R.P. Lewandowski, M. Wang, L.A. Bramble, G.R. Gookin, Z. Ning, M.T. Kleinman, C. Sioutas, A.E. Nel, Ambient ultrafine particles provide a strong adjuvant effect in the secondary immune response: implication for traffic-related asthma flares, Am. J. Physiol. Lung Cell. Mol. Physiol. 299 (2010) 18.
[8] A. Nel, T. Xia, L. Madler, N. Li, Toxic potential of materials at the nanolevel, Science 311 (2006) 622–627.
[9] C. Buzea, I.I. Pacheco, K. Robbie, Nanomaterials and nanoparticles: sources and toxicity, Biointerphases 2 (2007) MR17–MR71.
[10] A. Kroll, M.H. Pillukat, D. Hahn, J. Schnekenburger, Current in vitro methods in nanoparticle risk assessment: limitations and challenges, Eur. J. Pharm. Biopharm. 72 (2009) 370–377.
[11] A.E. Nel, L. Madler, D. Velegol, T. Xia, E.M.V. Hoek, P. Somasundaran, F. Klaessig, V. Castranova, M. Thompson, Understanding biophysicochemical interactions at the nano-bio interface, Nat. Mater. 8 (2009) 543–557.
[12] J. Rejman, V. Oberle, I.S. Zuhorn, D. Hoekstra, Size-dependent internalization of particles via the pathways of clathrin- and caveolae-mediated endocytosis, Biochem. J. 377 (2004) 159–169.
[13] S.K. Banerji, M.A. Hayes, Examination of nonendocytotic bulk transport of nanoparticles across phospholipid membranes, Langmuir 23 (2007) 3305–3313.
[14] N.R. Yacobi, L. DeMaio, J.S. Xie, S.F. Hamm-Alvarez, Z. Borok, K.J. Kim, E.D. Crandall, Polystyrene nanoparticle trafficking across alveolar epithelium, Nanomed. Nanotechnol. Biol. Med. 4 (2008) 139–145.
[15] C.M. Sayes, K.L. Reed, D.B. Warheit, Assessing toxicity of fine and nanoparticles: comparing in vitro measurements to in vivo pulmonary toxicity profiles, Toxicol. Sci. 97 (2007) 163–180.
[16] A. Villanueva, M. Canete, A.G. Roca, M. Calero, S. Veintemillas-Verdaguer, C.J. Serna, M.D. Morales, R. Miranda, The influence of surface functionalization on the enhanced internalization of magnetic nanoparticles in cancer cells, Nanotechnology 20 (2009).
[17] S. Patil, A. Sandberg, E. Heckert, W. Self, S. Seal, Protein adsorption and cellular uptake of cerium oxide nanoparticles as a function of zeta potential, Biomaterials 28 (2007) 4600–4607.
[18] O. Harush-Frenkel, N. Debotton, S. Benita, Y. Altschuler, Targeting of nanoparticles to the clathrin-mediated endocytic pathway, Biochem. Biophys. Res. Commun. 353 (2007) 26–32.
[19] A. Verma, F. Stellacci, Effect of surface properties on nanoparticle–cell interactions, Small 6 (2010) 12–21.
[20] N.R. Yacobi, N. Malmstadt, F. Fazlollahi, L. DeMaio, R. Marchelletta, S.F. Hamm-Alvarez, Z. Borok, K.J. Kim, E.D. Crandall, Mechanisms of alveolar epithelial translocation of a defined population of nanoparticles, Am. J. Respir. Cell Mol. Biol. 42 (2010) 604–614.
[21] C. Rossi, J. Chopineau, Biomimetic tethered lipid membranes designed for membrane–protein interaction studies, Eur. Biophys. J. Biophys. Lett. 36 (2007) 955–965.
[22] S.D. Conner, S.L. Schmid, Regulated portals of entry into the cell, Nature 422 (2003) 37–44.
[23] H.T. Tien, A. Ottova-Leitmannova, Membrane Biophysics as Viewed from Experimental Bilayer Lipid Membranes, Elsevier, New York, 2000.
[24] P. Nollert, H. Kiefer, F. Jahnig, Lipid vesicle adsorption versus formation of planar bilayers on solid-surfaces, Biophys. J. 69 (1995) 1447–1455.
[25] S.R. Jadhav, S.R. Kota, Y. Zheng, R.M. Garavito, R.M. Worden, Voltage dependent closure of PorB Class II porin from *Neisseria meningitidis* investigated using impedance spectroscopy in a tethered bilayer lipid membrane interface, J. Colloid Interface Sci. 390 (2013) 211–216.

[26] S.R. Jadhav, Y. Zheng, R.M. Garavito, R.M. Worden, Functional characterization of PorB class II porin from *Neisseria meningitidis* using a tethered bilayer lipid membrane, Biosens. Bioelectron. 24 (2008) 831–835.
[27] Y. Huang, Y. Liu, B.L. Hassler, R.M. Worden, A.J. Mason, A protein-based electrochemical biosensor array platform for integrated microsystems, IEEE Trans. Biomed. Circuits Syst. 7 (2013) 43–51.
[28] V.V. Ginzburg, S. Balijepailli, Modeling the thermodynamics of the interaction of nanoparticles with cell membranes, Nano Lett. 7 (2007) 3716–3722.
[29] A. Negoda, Y. Liu, W.C. Hou, C. Corredor, B.Y. Moghadam, C. Musolff, L. Li, W. Walker, P. Westerhoff, A.J. Mason, P. Duxbury, J.D. Posner, R.M. Worden, Engineered nanomaterial interactions with bilayer lipid membranes: a screening platform to assess nanoparticle toxicity, Int. J. Biomed. Nanosci. Nanotechnol. 3 (2013) 52–82.
[30] D. Napierska, L.C.J. Thomassen, D. Lison, J.A. Martens, P.H. Hoet, The nanosilica hazard: another variable entity, Part. Fibre Toxicol. 7 (2010).
[31] C.E. Ashley, E.C. Carnes, G.K. Phillips, D. Padilla, P.N. Durfee, P.A. Brown, T.N. Hanna, J. Liu, B. Phillips, M.B. Carter, N.J. Carroll, X. Jiang, D.R. Dunphy, C.L. Willman, D.N. Petsev, D.G. Evans, A.N. Parikh, B. Chackerian, W. Wharton, D.S. Peabody, C.J. Brinker, The targeted delivery of multicomponent cargos to cancer cells by nanoporous particle-supported lipid bilayers, Nat. Mater. 10 (2011) 389–397.
[32] S.-H. Wu, Y. Hung, C.-Y. Mou, Mesoporous silica nanoparticles as nanocarriers, Chem. Commun. 47 (2011) 9972–9985.
[33] Z. Li, J.C. Barnes, A. Bosoy, J.F. Stoddart, J.I. Zink, Mesoporous silica nanoparticles in biomedical applications, Chem. Soc. Rev. 41 (2012) 2590–2605.
[34] M. Ding, F. Chen, X.L. Shi, B. Yucesoy, B. Mossman, V. Vallyathan, Diseases caused by silica: mechanisms of injury and disease development, Int. Immunopharmacol. 2 (2002) 173–182.
[35] C.J. Johnston, K.E. Driscoll, J.N. Finkelstein, R. Baggs, M.A. O'Reilly, J. Carter, R. Gelein, G. Oberdorster, Pulmonary chemokine and mutagenic responses in rats after subchronic inhalation of amorphous and crystalline silica, Toxicol. Sci. 56 (2000) 405–413.
[36] M. Park, W. Annema, A. Salvati, A. Lesniak, A. Elsaesser, C. Barnes, G. McKerr, C.V. Howard, I. Lynch, K.A. Dawson, A.H. Piersma, W.H. de Jong, In vitro developmental toxicity test detects inhibition of stem cell differentiation by silica nanoparticles, Toxicol. Appl. Pharmacol. 240 (2009) 108–116.
[37] H. Zhang, D.R. Dunphy, X. Jiang, H. Meng, B. Sun, D. Tarn, M. Xue, X. Wang, S. Lin, Z. Ji, R. Li, F.L. Garcia, J. Yang, M.L. Kirk, T. Xia, J.I. Zink, A. Nel, C.J. Brinker, Processing pathway dependence of amorphous silica nanoparticle toxicity: colloidal vs pyrolytic, J. Am. Chem. Soc. 134 (2012) 15790–15804.
[38] B.D. Chithrani, W.C.W. Chan, Elucidating the mechanism of cellular uptake and removal of protein-coated gold nanoparticles of different sizes and shapes, Nano Lett. 7 (2007) 1542–1550.
[39] Y. Roiter, M. Ornatska, A.R. Rammohan, J. Balakrishnan, D.R. Heine, S. Minko, Interaction of nanoparticles with lipid membrane, Nano Lett. 8 (2008) 941–944.
[40] R. Naumann, D. Walz, S.M. Schiller, W. Knoll, Kinetics of valinomycin-mediated K^+ ion transport through tethered bilayer lipid membranes, J. Electroanal. Chem. 550 (2003) 241–252.
[41] T.N. Tun, A.T.A. Jenkins, An electrochemical impedance study of the effect of pathogenic bacterial toxins on tethered bilayer lipid membrane, Electrochem. Commun. 12 (2010) 1411–1415.
[42] P.N. Yaron, B.D. Holt, P.A. Short, M. Lösche, M.F. Islam, K.N. Dahl, Single wall carbon nanotubes enter cells by endocytosis and not membrane penetration, J. Nanobiotechnol. 9 (2011) 45.
[43] M.E. Orazem, B. Tribollet, Electrochemical Impedance Spectroscopy, John Wiley & Sons, Inc., 2008
[44] V. Freger, S. Bason, Characterization of ion transport in thin films using electrochemical impedance spectroscopy. I. Principles and theory, J. Membr. Sci. 302 (2007) 1–9.
[45] Z. Lukacs, Evaluation of model and dispersion parameters and their effects on the formation of constant-phase elements in equivalent circuits, J. Electroanal. Chem. 464 (1999) 68–75.
[46] G. Valincius, T. Meskauskas, F. Ivanauskas, Electrochemical impedance spectroscopy of tethered bilayer membranes, Langmuir 28 (2012) 977–990.
[47] D.B. Warheit, How meaningful are the results of nanotoxicity studies in the absence of adequate material characterization? Toxicol. Sci. 101 (2008) 183–185.
[48] R.C. Murdock, L. Braydich-Stolle, A.M. Schrand, J.J. Schlager, S.M. Hussain, Characterization of nanomaterial dispersion in solution prior to in vitro exposure using dynamic light scattering technique, Toxicol. Sci. 101 (2008) 239–253.
[49] G.W. Milligan, M.C. Cooper, A study of standardization of variables in cluster analysis, J. Classif. 5 (1988) 181–204.
[50] H. Shimodaira, An approximately unbiased test of phylogenetic tree selection, Syst. Biol. 51 (2002) 492–508.
[51] G.M. Ljung, G.E.P. Box, On a measure of lack of fit in time series models, Biometrika 65 (1978) 297–303.
[52] J.P. Royston, Algorithm AS 181: the W test for normality, J. R. Stat. Soc. C Appl. Stat. 31 (1982) 176–180.
[53] M.S. Bartlett, Properties of sufficiency and statistical tests, Proc. R. Soc. Lond. A Math. Phys. Sci. 160 (1937) 268–282.
[54] G.B. Sukhorukov, E. Donath, H. Lichtenfeld, E. Knippel, M. Knippel, A. Budde, H. Möhwald, Layer-by-layer self assembly of polyelectrolytes on colloidal particles, Colloids Surf., A Physicochem. Eng. Asp. 137 (1998) 253–266.
[55] K.J. Kwak, G. Valincius, W.C. Liao, X. Hu, X. Wen, A. Lee, B. Yu, D.J. Vanderah, W. Lu, L.J. Lee, Formation and finite element analysis of tethered bilayer lipid structures, Langmuir 26 (2010) 18199–18208.
[56] T. Cassier, A. Sinner, A. Offenhäuser, H. Möhwald, Homogeneity, electrical resistivity and lateral diffusion of lipid bilayers coupled to polyelectrolyte multilayers, Colloids Surf. B Biointerfaces 15 (1999) 215–225.
[57] A. Tekin, E. Hammond, Factors affecting the electrical resistivity of soybean oil methyl ester, J. Am. Oil Chem. Soc. 77 (2000) 281–283.
[58] S.R. Jadhav, D.X. Sui, R.M. Garavito, R.M. Worden, Fabrication of highly insulating tethered bilayer lipid membrane using yeast cell membrane fractions for measuring ion channel activity, J. Colloid Interface Sci. 322 (2008) 465–472.
[59] M. Montal, P. Mueller, Formation of bimolecular membranes from lipid monolayers and a study of their electrical properties, Proc. Natl. Acad. Sci. U. S. A. 69 (1972) 3561–3566.
[60] R. Campos, R. Kataky, Electron transport in supported and tethered lipid bilayers modified with bioelectroactive molecules, J. Phys. Chem. B 116 (2012) 3909–3917.
[61] J. Kang, P.A. Rowntree, Gold film surface preparation for self-assembled monolayer studies, Langmuir 23 (2007) 509–516.
[62] G. Dutta, K. Jo, H. Lee, B. Kim, H.Y. Woo, H. Yang, Time-dependent decrease in the enhanced electrocatalytic activities observed after three different pretreatments of gold electrodes, J. Electroanal. Chem. 675 (2012) 41–46.
[63] S.R. Jadhav, A.J. Needler, R.M. Worden, Interaction of polyamidoamine dendrimers with glassy carbon supported bilayer lipid membranes, NSTI Nanotech, vol. 1, Nano Science and Technology Institute, Boston, 2008, pp. 336–339.
[64] S.P. Hong, A.U. Bielinska, A. Mecke, B. Keszler, J.L. Beals, X.Y. Shi, L. Balogh, B.G. Orr, J.R. Baker, M.M.B. Holl, Interaction of poly(amidoamine) dendrimers with supported lipid bilayers and cells: hole formation and the relation to transport, Bioconjug. Chem. 15 (2004) 774–782.
[65] S.P. Hong, P.R. Leroueil, E.K. Janus, J.L. Peters, M.M. Kober, M.T. Islam, B.G. Orr, J.R. Baker, M.M.B. Holl, Interaction of polycationic polymers with supported lipid bilayers and cells: nanoscale hole formation and enhanced membrane permeability, Bioconjug. Chem. 17 (2006) 728–734.
[66] J.M. Chen, J.A. Hessler, K. Putchakayala, B.K. Panama, D.P. Khan, S. Hong, D.G. Mullen, S.C. DiMaggio, A. Som, G.N. Tew, A.N. Lopatin, J.R. Baker, M.M.B. Holl, B.G. Orr, Cationic nanoparticles induce nanoscale disruption in living cell plasma membranes, J. Phys. Chem. B 113 (2009) 11179–11185.
[67] B. Jing, Y. Zhu, Disruption of supported lipid bilayers by semihydrophobic nanoparticles, J. Am. Chem. Soc. 133 (2011) 10983–10989.
[68] M.R.R. de Planque, S. Aghdaei, T. Roose, H. Morgan, Electrophysiological characterization of membrane disruption by nanoparticles, ACS Nano 5 (2011) 3599–3606.
[69] J.L. Goldstein, M.S. Brown, R.G. Anderson, D.W. Russell, W.J. Schneider, Receptor-mediated endocytosis: concepts emerging from the LDL receptor system, Annu. Rev. Cell Biol. 1 (1985) 1–39.